Materials & Design 253 (2025) 113859

Contents lists available at ScienceDirect

Materials & Design

journal homepage: www.elsevier.com/locate/matdes

Resistance spot welded NiTi shape memory alloy to Ti6Al4V: Correlation between joint microstructure, cracking and mechanical properties

Yihu Zang [a], Jilin Xie [a,*], Yuhua Chen [a], Min Zheng [a], Xiaofang Liu [b], Jiajia Shen [c], J.P. Oliveira [c]

[a] Jiangxi Key Laboratory of Extreme Manufacturing Technology for High-end Equipment, Nanchang Hangkong University, Nanchang 330063, China
[b] State Key Laboratory of High Performance &Advanced Welding Materials, 450001, China
[c] CENIMAT/I3N, Departamento de Ciências dos Materiais, Faculdade de Ciências e Tecnologia, Universidade Nova de Lisboa, 2829-516 Caparica, Portugal

ARTICLE INFO

Keywords:
Resistance spot welded
NiTi shape memory alloy
Joint cracks
Brittle phase
Mechanical property

ABSTRACT

Despite the popularity of joining NiTi and Ti6Al4V in aerospace and biomedical applications, effective solutions for their dissimilar joining are limited due to brittle intermetallic compounds. In this work, we successfully joined NiTi/Ti6Al4V using resistance spot welding. Results indicate that the number of cracks is the primary factor determining the lap-shear load. The extensive accumulation of brittle Ti_2Ni at the bottom of the weld pool leads to stress concentration and is the main cause of crack initiation. X-ray diffraction and phase diagrams revealed the solidification sequence of liquid metal in the joint, including $L \rightarrow NiTi$, $L + NiTi \rightarrow Ti_2Ni$, $L \rightarrow \beta Ti + Ti_2Ni$. Electron backscatter diffraction analysis showed that weld nugget grains exhibited random orientation, with stress concentration mainly within the Ti_2Ni phase on the Ti6Al4V side and at the boundary between the NiTi and Ti_2Ni phases, contributing to high susceptibility to deformation and cracking in these regions. Nano-indentation analysis further demonstrated that the welding process diminished the superelastic performance of NiTi, attributable to Ti_2Ni phase, grain coarsening and the orientation deviation of B2 NiTi.

1. Introduction

Ni-Ti shape memory alloys (SMAs) are among the most widely used SMAs globally, attributed to their unique shape memory effect, superelasticity, and excellent biocompatibility. These attributes render them ideal for applications in medical devices, aerospace, and seismic damping systems [1–3]. Additionally, Ni-Ti alloys exhibit outstanding physical properties, fatigue resistance, and corrosion resistance, further enhancing their potential applications [4,5]. Conversely, Ti6Al4V alloy, the most commonly employed titanium alloy, is renowned for its high strength-to-weight ratio, excellent corrosion resistance, and biocompatibility. Consequently, it is widely utilized in aerospace, medical devices, chemical engineering, and civilian sectors [6,7]. The combination of NiTi and Ti6Al4V alloys enables the integration of their superior properties, reduces the weight of the alloy composition, and enhances the strength and deformation capabilities of the NiTi/Ti6Al4V dissimilar joints under extreme conditions [8]. This synergy improves the thrust-to-weight ratio and energy absorption properties of spacecraft, significantly advancing the aerospace industry [9].

Weldability, as a crucial metric, reflects the ability to achieve high-quality joints through welding processes [10]. However, discrepancies in the physical and chemical properties of materials pose challenges in welding dissimilar materials, including poor weld formation, narrow processing windows, and low joint strength. NiTi/Ti6Al4V dissimilar joints also face these issues, making it difficult to meet industrial requirements.

To address these challenges, various methods have been explored. To date, research on welding methods for NiTi/Ti6Al4V dissimilar materials mainly includes brazing, fusion welding, and solid-state welding. Among these, brazing was the earliest method studied for joining NiTi/Ti6Al4V alloys. Quintino et al. [11] successfully joined NiTi/Ti6Al4V dissimilar alloys using Bag-8 as a filler, but the mechanical properties of the joints were suboptimal. Laser welding, a representative fusion welding method characterized by its high energy density and low heat input, has been extensively applied to the joining of various dissimilar alloys. Numerous studies on NiTi/Ti6Al4V dissimilar joints have employed laser welding with butt joints, lap joints, or intermediate layers to modulate the weld composition. For instance, Miranda et al. [12] achieved successful butt joint welding of NiTi/Ti6Al4V dissimilar alloys but observed numerous cracks in the heat-affected zone. Song et al. [13] used laser lap welding to directly join NiTi alloys to Ti6Al4V alloys; however, X-ray analysis revealed a significant presence of brittle

* Corresponding author.
E-mail address: xiejilin1990@126.com (J. Xie).

https://doi.org/10.1016/j.matdes.2025.113859
Received 30 December 2024; Received in revised form 28 February 2025; Accepted 19 March 2025
Available online 21 March 2025

Ti_2Ni intermetallic compounds in the welds. Zhou et al. [14] employed Nb wire as an intermediate layer to laser-weld TiNiNb alloys to Ti6Al4V alloys. Despite this, Ti_2Ni intermetallic compounds were still detected at the joints due to direct contact between the base materials. Oliveira et al. [9] successfully joined NiTi and Ti6Al4V alloys using high-melting-point Nb as a filler and a laser offset method, avoiding the formation of titanium-nickel intermetallic compounds. However, precise control of laser offset, a critical factor for achieving high-quality welds, remains challenging. Solid-state welding methods such as diffusion welding and ultrasonic spot welding, characterized by the absence of melting in the base materials, have also been explored for dissimilar material joining. Simões et al. [15] applied diffusion welding using Ti/Ni multilayer films deposited by magnetron sputtering as filler materials to join NiTi and Ti6Al4V alloys, but Ti_2Ni formation and low mechanical properties were observed in the joints. Xie et al. [16] investigated the feasibility of ultrasonic spot welding for NiTi and Ti6Al4V alloys by electroplating aluminum on Ti6Al4V. However, this process was relatively complex, and a thick $TiAl_3$ intermetallic compound layer formed between Ti6Al4V and the aluminum coating.

Based on Joule's Law, the core principle of resistance spot welding (RSW) is to utilize the heat generated by an electric current passing through the workpieces to achieve the materials joining. Compared to other welding methods, RSW offers several distinct advantages for joining NiTi shape memory alloy and Ti6Al4V titanium alloy. These advantages include stable weld quality, extremely short production cycles, environmental friendliness, and strong process controllability. For instance, RSW can be automated to achieve consistent and repeatable welds without the need for shielding gases. Moreover, considering the different melting points, electrical resistivities, thermal conductivities, and hardness values of the materials to be welded, RSW demonstrates unique capabilities in controlling the dynamic behavior of dissimilar metals. This is especially true when the geometry of the electrodes can be further optimized for different material combinations, highlighting the flexibility inherent in joining dissimilar materials [17,18]. These unique advantages of RSW have led to its widespread application in aerospace, automotive manufacturing, and electronics industries [19,20].

It is well-known that the formation of intermetallic compounds is evidence of metallurgical reactions in welded joints. Zhang et al. [21] proposed that longer welding times result in higher welding temperatures, which are conducive to the growth of reaction layers in dissimilar metal joints — a condition that RSW can readily achieve. Additionally, the three-phase secondary rectifier welding machine used in our experiments features independent parameters for preheating current, welding current, post-heating current, preheating time, welding time, and post-heating time. These parameters can be fine-tuned to complement each other, providing maximum convenience and feasibility for the growth of reaction layers in dissimilar joints.

Given the above discussions, applying RSW to NiTi/Ti6Al4V dissimilar alloy research holds significant promise. Although the connection of these materials has been explored using other welding methods, no comprehensive solution exists to date. Furthermore, to the best of the authors' knowledge, no published literature addresses RSW for NiTi/Ti6Al4V dissimilar alloys. In this study, the RSW process was successfully employed to join NiTi and Ti6Al4V dissimilar alloys. The elemental distribution, phase composition, crystal structure, and microstructural evolution across different regions of the dissimilar joints were characterized and analyzed. Corresponding mechanical properties were also evaluated to investigate the phase evolution process in RSW joints and explore the influence of various phases on joint microhardness and superelastic properties.

2. Experiment

2.1. Materials and methods

The NiTi alloy used in this study was provided by Beijing SMA Technology and Trade Co., Ltd., while the Ti6Al4V alloy was supplied by the Northwest Institute for Nonferrous Metal Research. The NiTi base material (BM) primarily consisted of the NiTi (B2 austenite) phase, and the Ti6Al4V BM was in a rolled and annealed state, featuring both α-Ti and β-Ti phases (Fig. 1a). This dual-phase composition endows the Ti6Al4V BM with the combined advantages of α- and β-titanium alloys. The chemical compositions of the BMs are shown in Table 1.

The NiTi alloy surface was covered by a dense oxide layer, which was removed prior to welding using a solution composed of HF, HNO_3, and H_2O in a volume ratio of 1 : 3 : 5 The Ti6Al4V alloy surface was ground with silicon carbide sandpaper to ensure a proper overlap for welding. Both materials were subsequently cleaned with alcohol and air-dried for use. The experiment employed a lap joint configuration, where the NiTi alloy overlapped the Ti6Al4V alloy. Copper-chromium-zirconium alloy was used for the electrodes. To achieve symmetric nugget formation at the joint interface, a spherical electrode was applied on the NiTi side, while a flat electrode was used on the Ti6Al4V side. The schematic of the lap joint configuration is illustrated in Fig. 1b. The welding equipment was a KDWJ-17 three-phase secondary rectifier resistance welding machine with a rated power of 300 kW. The coordination of parameters across various stages of the RSW process is detailed in Fig. 1c ($1 cycle = 20 ms$).

2.2. Sample preparation and characterization

After welding, the joints were sectioned along the weld centerline using wire-cut electrical discharge machining (EDM) to obtain metallographic samples. These samples were ground with progressively finer sandpapers and polished to a mirror finish. To investigate the microstructural evolution within the joint, a Phenom-XL-SED scanning electron microscope (SEM) equipped with an energy dispersive spectrometer (EDS) was used to observe and analyze the microstructure and fracture surfaces of the dissimilar joint. Phase compositions of the base materials and the dissimilar joint were determined using a Rigaku Rapid IIR X-ray diffractometer (XRD). Electron backscatter diffraction (EBSD) was utilized to observe the grain morphology and stress/strain distribution across the joint cross-section. The sample surface was polished using argon ion polishing to eliminate residual stress, with a step size of 0.2 μm. The NiTi/Ti6Al4V interface was characterized using an FEI Talos transmission electron microscope (TEM) operated at 200 kV. TEM samples were prepared using focused ion beam (FIB) techniques. To assess the impact of the RSW process on the superelasticity of the NiTi alloy, nanoindentation testing was performed using a nanoindenter (NI) with a load of 3 mN, a loading rate of 600 μN/s, and a dwell time of 2 s. The joint strength of the NiTi/Ti6Al4V dissimilar welds was evaluated through tensile testing at room temperature using a WDS-1000 universal testing machine. Tensile tests were conducted at a displacement rate of 1 mm/min. Prior to testing, spacers of identical thickness were added to both ends of the joint to ensure that the loading axis was parallel to the shear plane. To ensure the reliability of the tensile results, the data for each joint were averaged from three individual samples.

3. Results

3.1. Relationship between mechanical properties, cracks and the secondary Ti_2Ni phase

Fig. 2 illustrates the mechanical properties of the NiTi/Ti6Al4V dissimilar joints, including the load–displacement curves (Fig. 2a) and the statistical results of tensile-shear strength (Fig. 2b).

As shown in Fig. 2(a) and (b), the load–displacement curve exhibits a

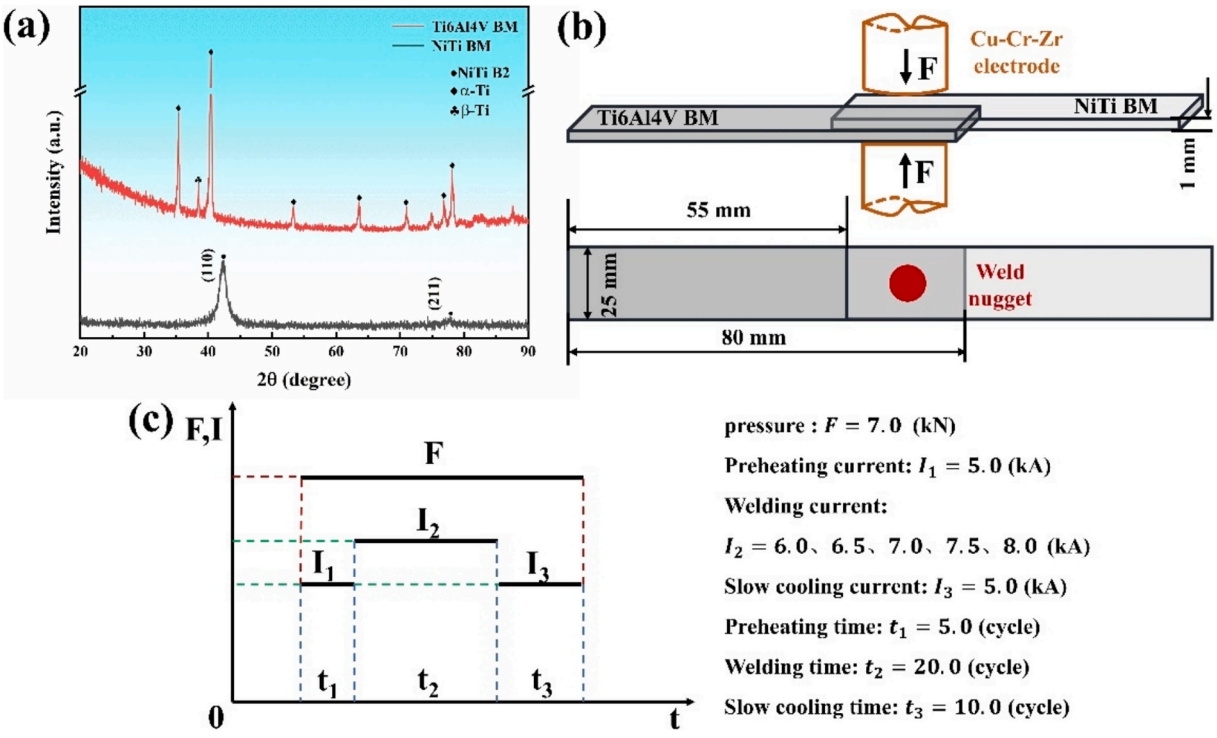

Fig. 1. (a) XRD patterns of the NiTi and Ti6Al4V BMs; (b) Schematic diagram of RSW assembly and (c) Process of RSW coordination of parameters in each stage.

Table 1
Chemical composition of BM in the study (wt, %).

	Al	Ni	V	O	N	H	Fe	C	Ti
NiTi	–	55.66	–	0.05	–	–	–	0.05	Bal.
Ti6Al4V	6.0	–	4.0	0.06	0.008	0.007	0.026	0.015	Bal.

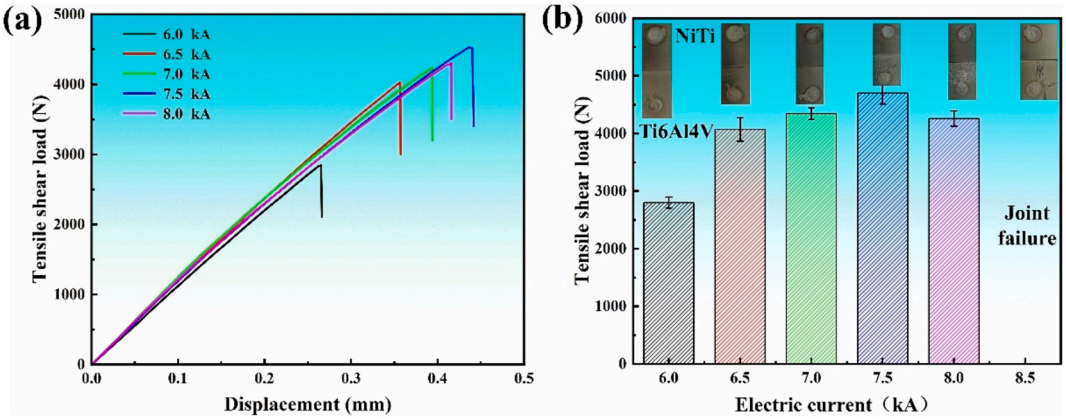

Fig. 2. (a) Load displacement graph and (b) Tensile shear strength statistics.

trend of initial increase followed by a decrease. The joint strength reaches its maximum at a welding current of 7.5 kA, with a tensile-shear load of 4703 N. Conversely, the minimum tensile-shear load of 2800 N is observed at a welding current of 6.0 kA. No test data are available for the 8.5 kA condition due to excessive spattering, which caused joint failure and invalidated the weld.

Fig. 3 presents the complete cross-sectional morphology (highlighted in blue) and the corresponding crack statistics of NiTi/Ti6Al4V dissimilar joints under the RSW process. Observations from Fig. 3(a-e) show that both the NiTi and Ti6Al4V base materials (BMs) exhibit minor deformation and a distinct hump-shaped weld nugget is formed on the NiTi plate. Multiple cracks are also observed at the NiTi/Ti6Al4V joint interface, with variations in crack number and the weld nugget length ratio under different parameters. Statistical Analysis from Fig. 3(f) show that at a welding current of 7.5 kA, the number of cracks is minimized to 10. The ratio of the weld nugget length to the joint connection length is nearly the highest, approximately 73 %.

The experimental results confirm that the minimal crack count and maximal mechanical performance is observed at 7.5 kA demonstrate the critical role of cracks in affecting joint integrity and strength [22]. These findings validate that 7.5 kA is the optimal current parameter in this study.

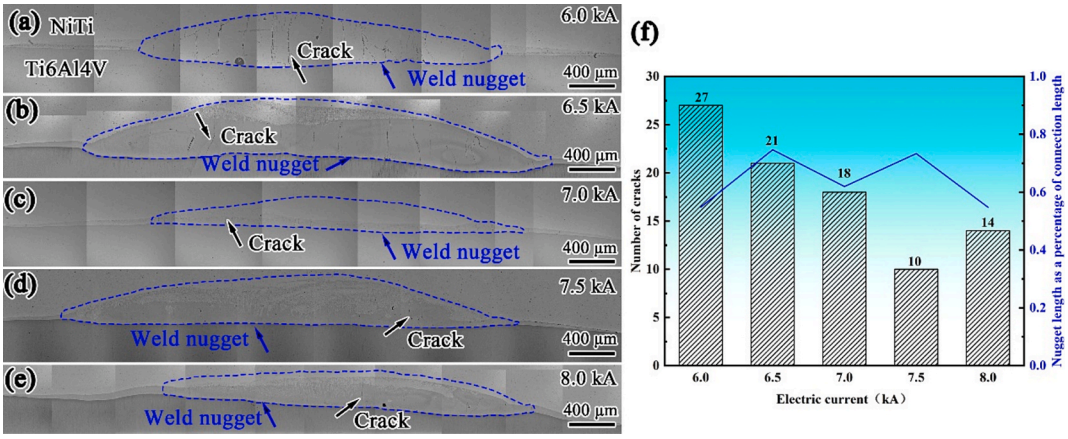

Fig. 3. (a-e) Weld appearance of NiTi/Ti6Al4V RSWed joint and (f) Cracking statistics chart.

The following section focuses on the key factors influencing the cracks in this experiment. Fig. 4 illustrates representative cracked regions under different parameters, displaying varying sizes and morphologies.

In Fig. 4(a), transverse cracks are observed to traverse the entire hump-shaped weld nugget at 6.0 kA, with relatively large widths. These cracks are hypothesized to result from electrode pressure, shrinkage voids, and the inherent brittleness of the weld nugget [23]. Longitudinal cracks are typically found between two transverse cracks, often interconnected. According to Griffith's critical condition for crack propagation, longitudinal cracks are a result of the combined effect of adjacent cracks [24]. In Fig. 4(b) and (c), transverse cracks are observed to originate at the fusion line on the Ti6Al4V interface and terminate at the columnar grains in the center of the weld nugget, with crack widths of less than 2 μm. Although some short longitudinal cracks are present in Fig. 4(b) (6.5 kA), their length and width are significantly smaller than those in Fig. 4(a). These are likely microcracks induced by the brittleness of the weld nugget and residual stresses [25–27]. Notably, these transverse cracks almost entirely disappear near the columnar grains at the center of the weld nugget, a phenomenon that is particularly evident at 7.5 kA (Fig. 4c). Fig. 4(e) and 4(f) show magnifications of areas A and B from Fig. 4(c).

Due to the brittleness of the fusion zone (FZ), transverse cracks propagate toward the center, but do not cross the entire weld nugget, with their width generally decreasing. Additionally, fine, leaf-shaped cracks are observed along the edges of the transverse cracks (Fig. 4e and f). These cracks exhibit branching, which can increase the number of crack surfaces and help release stress within the weld nugget [28]. At 7.5 kA, almost no longitudinal cracks are observed, indicating that transverse cracks are the primary factor affecting the joint's mechanical performance.

An interesting phenomenon is also observed in Fig. 4(a-d), where the proportion of the second phase (black phase, to be described later) first decreases and then increases under different parameters. The lowest proportion occurs at 7.5 kA, which contrasts with the mechanical performance trend in Fig. 2 and the crack number trend in Fig. 3(b). The microscopic morphology of cracks and their trends, along with the proportion of the second phase and mechanical performance, further suggest that both cracks and the second phase are significant factors affecting the experimental results. Therefore, an analysis of the

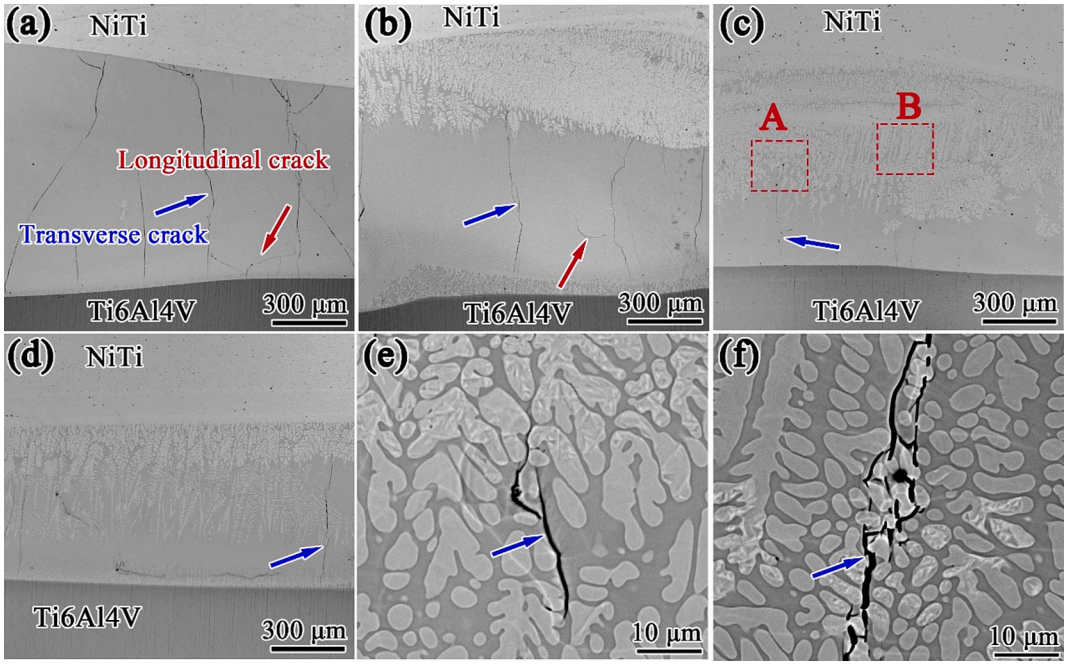

Fig. 4. Representative crack results (a) 6.0 kA, (b) 6.5 kA, (c) 7.5 kA, (d) 8.0 kA, (e) and (f) are enlarged views of regions A and B in (c) respectively.

microstructure of the joints at 7.5 kA is necessary to clarify the relationship between cracks, the second phase (Ti_2Ni), and mechanical properties.

3.2. Microstructure relationship between cracks and the Ti_2Ni second phase

The bonding state between dissimilar metals significantly influences the overall performance of the joint. In this experiment, the joint consists of two distinct regions: a bright region resembling the color of the NiTi alloy and a dark region resembling the color of the Ti6Al4V alloy. Therefore, the microstructure of the joint was analyzed using SEM and EDS measurements (the EDS results of the different points analyzed in Fig. 5 are listed in Table 2).

Fig. 5 presents a local magnified view of the joint at 7.5 kA, where it is observed that in areas without cracks, a strong metallurgical bond occurs at the interface between NiTi and Ti6Al4V, with no visible porosity or inclusions (Fig. 5 a and b). The weld nugget on the NiTi side primarily consists of equiaxed grains at the boundary of the base material and columnar grains at the center of the weld, while the Ti6Al4V side primarily exhibits a columnar grain structure. According to classical undercooling theory [29], during the solidification process, equiaxed grains transform into columnar grains with increasing G/R (where G is the temperature gradient and R is the growth rate). Considering the water-cooled electrodes on both sides, this transformation from equiaxed to columnar grains is acceptable.

EDS point analysis results show that the bright region (points 2–3 in Fig. 5a) corresponds to the NiTi phase, while the dark region (point 4) corresponds to the Ti_2Ni phase (second phase). In Fig. 5(b), a small crack is observed, originating at the fusion line on the Ti6Al4V side and propagating towards the center of the weld, stopping near the bright white NiTi phase. A detailed analysis reveals that the crack root exhibits transgranular fracture, which will be discussed in Section 3.3 on fracture morphology. EDS analysis indicates that the crack root region (point 5) and the middle region (points 6, 7) contain higher levels of Ti compared to Ni, with a Ti/Ni ratio close to 2:1, confirming the presence of the brittle Ti_2Ni intermetallic compound [30,31]. The higher Ti content in points 5–7 is due to the proximity to the Ti6Al4V base material, as Ti6Al4V melts into the weld nugget during the RSW process, dominating the Ti content. The extensive accumulation of Ti_2Ni phase is highly susceptible to stress concentration, becoming a source of crack initiation under external forces. Therefore, once a crack forms in the Ti_2Ni accumulation area, the intermetallic phase provides a preferential direction for crack propagation, which is the direct cause of the ease of crack formation on the Ti6Al4V side.

Fig. 5(c) shows the crack tip, which is primarily composed of a network-like distribution of Ti_2Ni and NiTi phases. As the crack propagates in this region, it usually exhibits branching, resulting in intergranular brittle fracture. This not only increases the number of fracture surfaces but also facilitates the release of stress in the weld. EDS results for points 7 and 8 in Fig. 5 correspond to the NiTi and Ti_2Ni phases, respectively. An important observation in this figure is that the crack originates in the Ti_2Ni phase on the Ti6Al4V side, slows or terminates at the NiTi phase in the center of the weld nugget, which will be further demonstrated in subsequent sections.

Table 2
EDS spot scan results.

Position	Ni	Ti	Al	V	Possible phase
1	53.22	46.78	–	–	NiTi BM
2	52.07	47.12	0.64	0.12	NiTi
3	51.56	47.42	1.02	–	NiTi
4	34.91	61.89	2.83	0.37	Ti_2Ni
5	33.5	60.79	4.83	0.88	Ti_2Ni
6	33.48	61.47	4.12	0.93	Ti_2Ni
7	34.37	59.87	4.62	1.14	Ti_2Ni
8	–	84.53	8.76	6.71	Ti6Al4V BM
9	51.32	47.2	1.31	0.17	NiTi
10	35.11	61.03	3.22	0.64	Ti_2Ni

The average free path of each element's diffusion into a given region is limited by the temperature achieved during the welding process and the duration of diffusion [32]. The bonding state of the NiTi/Ti6Al4V dissimilar joint was further analyzed from the perspective of element diffusion. Fig. 6(b-c) present the results of EDS area and line scans, showing an increase in the concentrations of Ti, Al, and V elements from top to bottom, while the Ni concentration gradually decreases. Additionally, the diffusion extent of Al and V elements is observed to be smaller than that of Ni and Ti. According to Fick's first law, atoms diffuse from regions of high concentration to low concentration, with the atomic flux being directly proportional to the mass concentration. This results in faster diffusion of high-concentration Ti and Ni elements compared to the slower diffusion of lower-concentration Al and V elements. A significant fluctuation in the EDS line scan curve is observed at the center of the weld nugget, with a length of approximately 300 μm (Fig. 6c). This indicates strong mixing of Ni and Ti elements at this location, with the Ti_2Ni and NiTi phases interwoven, reflecting a high degree of metallurgical bonding. The line scan results also confirm the formation of a substantial amount of Ti_2Ni on the Ti6Al4V side, consistent with the point analysis results shown in Fig. 5.

Tang et al. [33] studied the diffusion behavior of elements in nickel-based and iron-based coatings during the CMT process and found that elements with higher concentrations in the coating were difficult to diffuse into the substrate. A similar phenomenon is observed near the Ti6Al4V interface in Fig. 6(b-c), where Ni shows limited diffusion, possibly due to its relatively low diffusion coefficient on the Ti6Al4V side. Similarly, according to Fick's first law, a smaller diffusion coefficient results in lower atomic flux [34], which explains the relatively low Ni content diffusing into the Ti6Al4V side. Furthermore, during the RSW process, excessive heat input and the lower boiling point of Ni compared to Ti (boiling points: Ni 2913 °C, Ti 3287 °C) cause some Ni to evaporate, further reducing the amount of Ni diffusing into the Ti6Al4V side. An

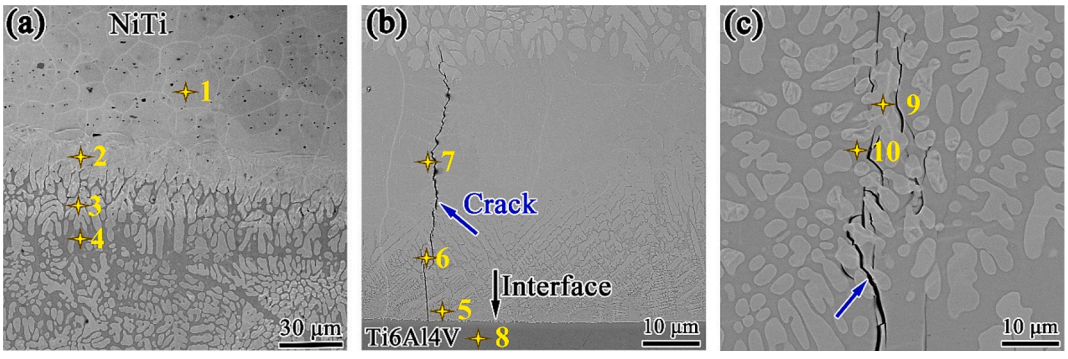

Fig. 5. (a-c) SEM micrographs of the 7.5 kA joints.

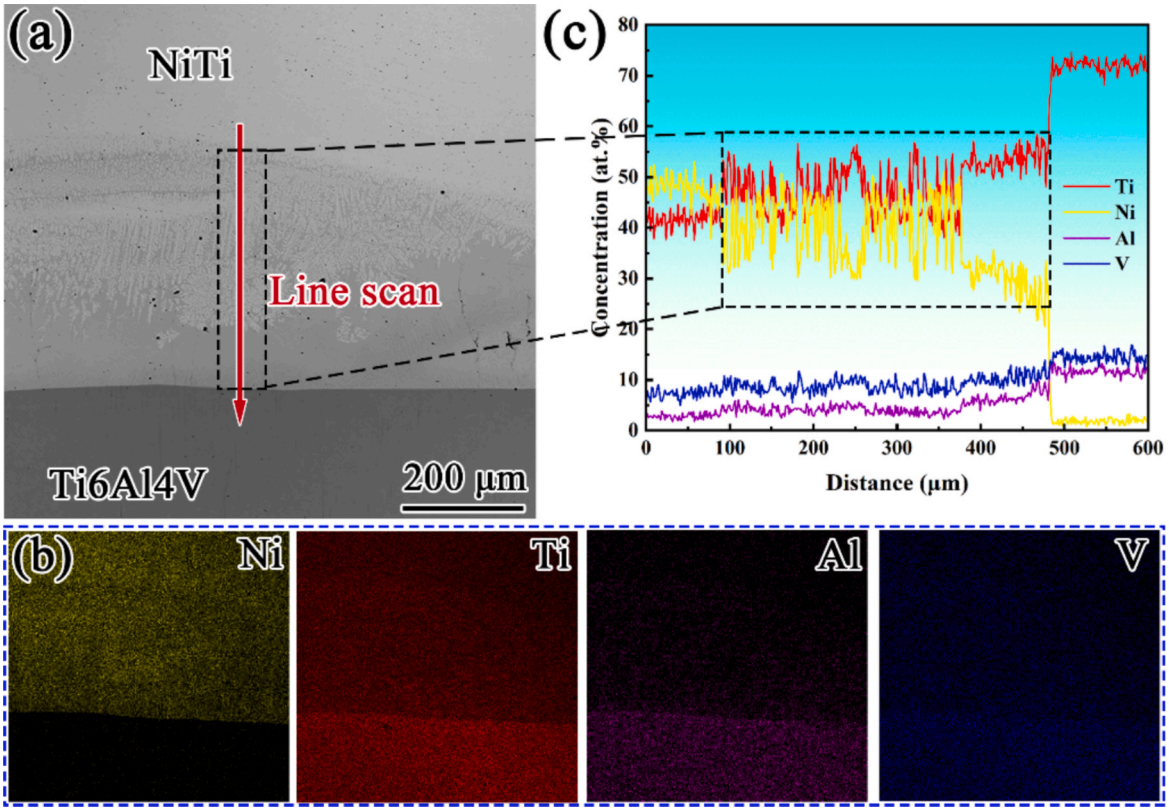

Fig. 6. (a) Face scan result and (b) line scan result of 7.5 kA joint.

interesting phenomenon is also observed in the line scan results. Although the Ti6Al4V base material has a higher Al content than V, the V concentration is almost always higher than that of Al throughout the line scan analysis. This may be attributed to the lower melting and boiling points of Al, leading to evaporation and burnout, a phenomenon also noted by Jiang et al. [8].

3.3. Fractography

The fracture surface and corresponding EDS analysis are shown in Fig. 7 and Table 3. Two distinct regions were observed on both the NiTi side (Fig. 7a and b) and the Ti6Al4V side (Fig. 7a and b). One region exhibited a relatively flat, smooth fracture surface with river patterns and cleavage steps. It is generally believed that river patterns and steps form when cracks propagate through screw dislocations; as the steps move in the same direction, many small steps gradually merge into larger ones. The other region was rough and contained fine fragmented particles, with both regions exhibiting clear brittle fracture characteristics. Point scan analysis of these regions revealed that the smooth blocky areas were primarily composed of the Ti_2Ni phase, while the particulate regions contained NiTi phase. Li et al. [35] also reported that Ti_2Ni and other Ni-Ti-based intermetallic compounds (IMCs) could embrittle the joint. During the brittle fracture process, the blocky Ti_2Ni phase fractures, and the residual Ti_2Ni phase embeds into the fracture surface, forming rough fragments. Additionally, as the content of Ti_2Ni phase increases, the proportion of intergranular brittle fracture in the fracture mode also increases [36]. Moreover, cracks that pass through the grains were observed in the smooth regions (Fig. 7b, d), which is due to crack propagation within the Ti_2Ni phase accumulation zone, consistent with the increased occurrence of transgranular cracking on the Ti6Al4V side. These observations indicate that the failure and fracture of the NiTi/Ti6Al4V dissimilar joint are primarily caused by the large volume of Ti_2Ni intermetallic compounds present in the joint.

4. Discussion

4.1. Properties of phases and phase transition behavior

To determine the phase composition and evolution process of the NiTi/Ti6Al4V dissimilar joint, X-ray diffraction (XRD) analysis was performed on joints with five different parameters. The results are shown in Fig. 8(a). All joints exhibited the presence of α-Ti, β-Ti, NiTi (B2), and Ti_2Ni phases, with the appearance of the Ti peak possibly resulting from the incorporation of excess Ti in the weld nugget. It was also observed that the intensity of the Ti_2Ni peak gradually decreased with increasing current, indicating a reduction in the Ti_2Ni content within the weld nugget as the current increased. Since Ti_2Ni is a brittle phase with a relatively low melting point, it is prone to welding cracks even under low stress, which explains the decrease in mechanical performance when Ti_2Ni content is higher [37]. Upon closer inspection, it was noted that the diffraction peak intensity of the Ti2Ni phase in the 7.5 kA joint was higher than that in the 8.0 kA joint, but the actual mechanical performance of 8.0 kA joint was relatively lower, possibly due to the smaller weld nugget area or more cracks at 8.0 kA. Fo r the NiTi and Ti_2Ni phases, their formation enthalpies can be estimated using the standard bivariate model [30,38]. Based on the Ti-Ni phase diagram (Fig. 8b), the basic reaction equations and corresponding formation enthalpies for NiTi and Ti_2Ni are as follows [28]:

$$Ni + Ti \rightarrow NiTi,\ -66.94\text{KJ/mol} \quad (1)$$

$$Ni + Ti \rightarrow Ti_2Ni,\ -100.35\text{KJ/mol} \quad (2)$$

The standard formation enthalpies of NiTi and Ti_2Ni phases are −66.94 kJ/mol and −100.35 kJ/mol, respectively. The equation for calculating the Gibbs free energy during the phase transformation is given by equation (3).

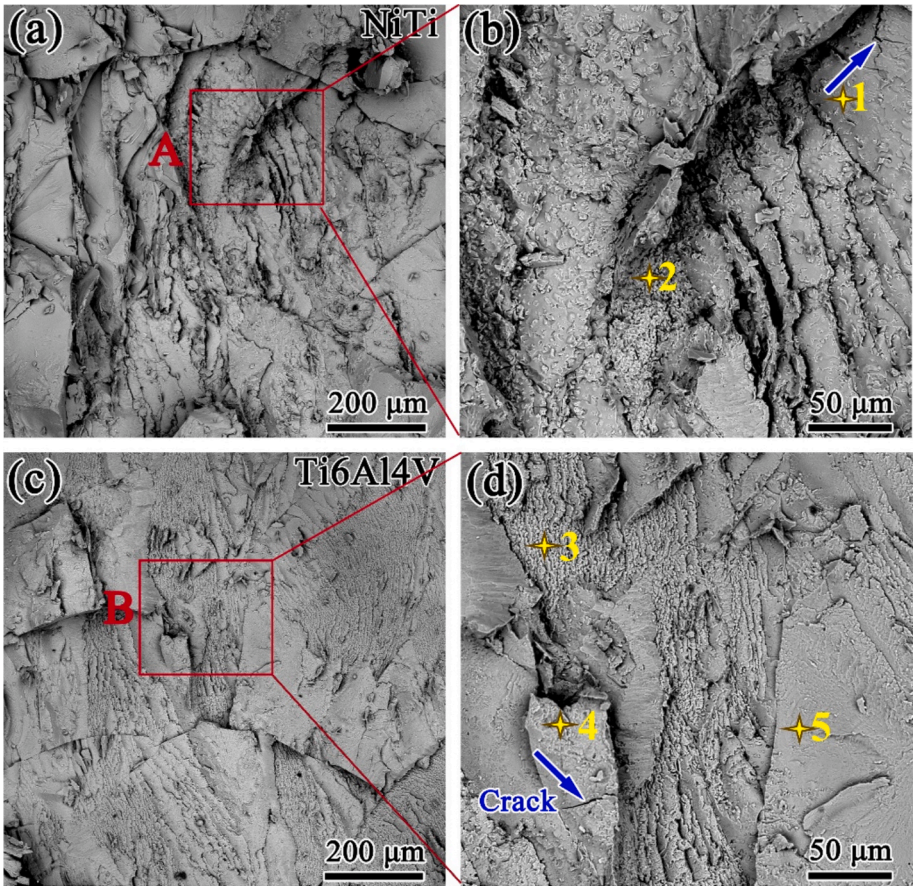

Fig. 7. SEM images of 7.5 kA joint fracture (a-b) NiTi side fracture, (b) is an enlarged view of region A in (a), (c-d) Ti6Al4V side fracture, (d) is an enlarged view of region B in (c).

Table 3
EDS point scan results for the fracture.

Position	Ni	Ti	Al	V	Possible phase
1	3429	62.63	3.08	–	Ti_2Ni
2	42.53	51.46	–	6	NiTi
3	12.97	71.86	11.83	3.34	Ti_2Ni + NiTi
4	23.14	67.38	9.48	–	Ti_2Ni
5	27.94	63.87	8.19	–	Ti_2Ni

$$\Delta G = \Delta H - T\frac{\Delta H}{T0} = \Delta H\frac{T0 - T}{T0} = \Delta H\frac{\Delta T}{T0} \tag{3}$$

In the equation, ΔG represents the Gibbs free energy, ΔH is the heat of transformation, ΔT is the temperature drop, and T_0 is the equilibrium phase transition temperature. According to the thermodynamics of compound formation, phase transitions can occur spontaneously. Furthermore, the Gibbs free energy of Ti_2Ni is lower than that of NiTi [39,40], such that $\Delta G1(Ti_2Ni) < \Delta G2(NiTi)$. Therefore, during the solidification process, the Ti_2Ni phase forms before the NiTi phase [41]. To further understand the solidification sequence of the liquid metal in the joint, the phase formation process of NiTi and Ti_2Ni in the weld pool is

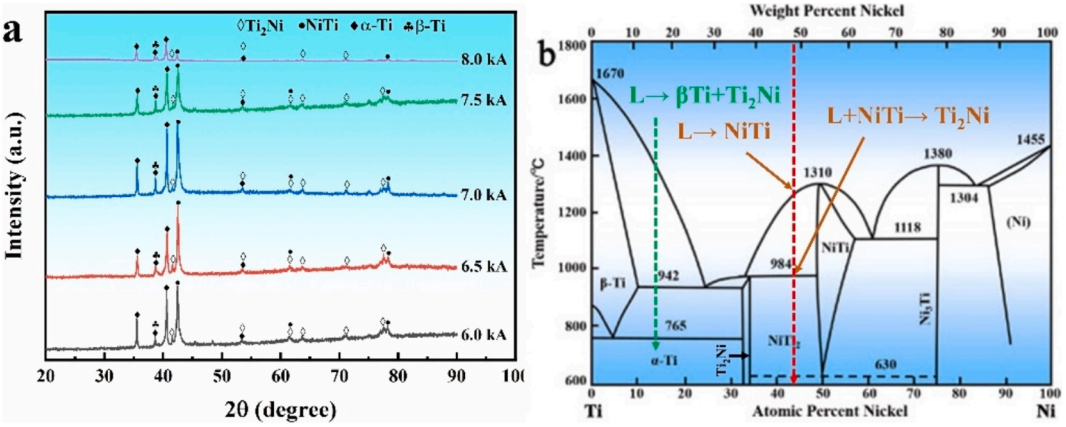

Fig. 8. (a) XRD results and (b) Ti-Ni binary phase diagram of RSW process at different welding parameters.

described according to the Ti-Ni binary phase diagram.

First, the NiTi phase forms at a higher temperature through a congruent reaction ($L \rightarrow NiTi$), resulting in a columnar dendritic structure in the joint microstructure. As the temperature decreases, a peritectic reaction ($L + NiTi \rightarrow Ti_2Ni$) occurs, forming the Ti_2Ni phase adjacent to the NiTi phase. Finally, as the temperature continues to decrease, an eutectic reaction ($L \rightarrow \beta Ti + Ti_2Ni$) takes place. Chen et al. [28] observed similar behavior in the laser joining of NiTiNb to Ti6Al4V, where a significant amount of brittle Ti_2Ni phase remained in the solidified weld. Consequently, the solidification process of the joint in the RSW process aligns with the X-ray diffraction results, leading to the following conclusion:

$L \rightarrow NiTi$(congruent reaction),

$L + NiTi \rightarrow Ti_2Ni$(peritectic reaction),

$L \rightarrow \beta Ti + Ti_2Ni$(eutectic reaction),

4.2. NiTi side interface and Ti6Al4V side interface

Based on the Ti-Ni phase diagram (Fig. 8b), a detailed analysis of the microstructure at the NiTi FZ interface and Ti6Al4V FZ interface was conducted. Fig. 9 shows STEM images of the NiTi-side interface, where three distinct phases are observed at different locations, labeled as 1, 2, and 3 (Fig. 9**a and b**). The diffraction spot numbers correspond to the respective locations, with results shown in Fig. 9(b-d). Selected area diffraction (SAD) at points 1 and 2 confirms the presence of a Ti_2Ni phase in the NiTi-side weld pool. The Ti required for the formation of Ti_2Ni comes from the melting of the NiTi base material (BM) and the significant amount of Ti entering the weld pool. As discussed in Section 4.1, the formation enthalpy of the Ti_2Ni phase is lower than that of NiTi, making the formation of Ti_2Ni easier. Therefore, the presence of Ti_2Ni in the NiTi-side weld pool is acceptable. Point 3 is located closer to the NiTi-side interface, where the diffraction pattern (Fig. 9**d**) corresponds to the NiTi phase. This suggests that at the interface, which is outside the weld pool and near the NiTi BM, the formation of Ti_2Ni is limited. As described in the joint microstructure in Fig. 5a, the NiTi-side weld pool contains a large amount of NiTi phase.

TEM-EDS observations show a significant gradient of elements, such as Ni and Ti, between the NiTi-side interface and the weld pool (Fig. 9**e** and h). The surface scan results further support these diffraction patterns.

Fig. 10(a and b) shows the STEM images of the Ti6Al4V FZ interface and the corresponding diffraction patterns for the selected areas. SAD results indicate that points 1–3 correspond to the face-centered cubic (FCC) Ti_2Ni phase, consistent with the point scan results shown in Fig. 5 (b). TEM-EDS analysis (Fig. 10e and h) reveals the presence of Ni elements at the Ti6Al4V-side interface, with a clear layer structure. Combined with the TEM results for the NiTi-side interface (Fig. 9), it is inferred that the entire weld pool contains significant amounts of Ni, Ti, Al, and V. This supports the mixing of different molten metals and the formation of intermetallic compounds [42]. Furthermore, the relatively large diffusion distances of dissimilar metal elements also contribute to enhancing the metallurgical bonding strength of the joint [43].

4.3. Weld formation mechanism

To further investigate the crystallographic characteristics of the NiTi/Ti6Al4V dissimilar joint, an EBSD analysis was performed, and the results are shown in Fig. 11. Due to the non-equilibrium solidification conditions, different grain growth morphologies and sizes were observed within the weld pool. The inverse pole figure (IPF) reveals a random grain orientation within the joint, with fine columnar grains observed in the NiTi-side weld pool, while coarser columnar grains are present on the Ti6Al4V-side (Fig. 11a). This columnar structure in the weld pool was formed during the RSW process by melting and rapid cooling. The lower thermal conductivity of the Ti6Al4V BM compared to the NiTi BM results in a slower solidification rate on the Ti6Al4V side, with a higher G/R value. Based on the grain morphology selection diagram provided by Lee et al. [44], the Ti6Al4V-side weld pool exhibits larger columnar grains. Fig. 11(b and c) show the pole figures (PF) of the NiTi and Ti_2Ni phases in the $<001>$、$<011>$ and $<111>$ directions. The maximum uniform density multiplication (MUD) value for Ti_2Ni is significantly higher than that for NiTi ($32.92 > 13.48$), indicating that the texture of Ti_2Ni is stronger in the $<001>$ direction. This is consistent with the arrows in Fig. 11(a), where the columnar grains on the Ti6Al4V side show a pronounced $<001>$ orientation. The reason for this is that Ti_2Ni belongs to the FCC structure, and the preferred

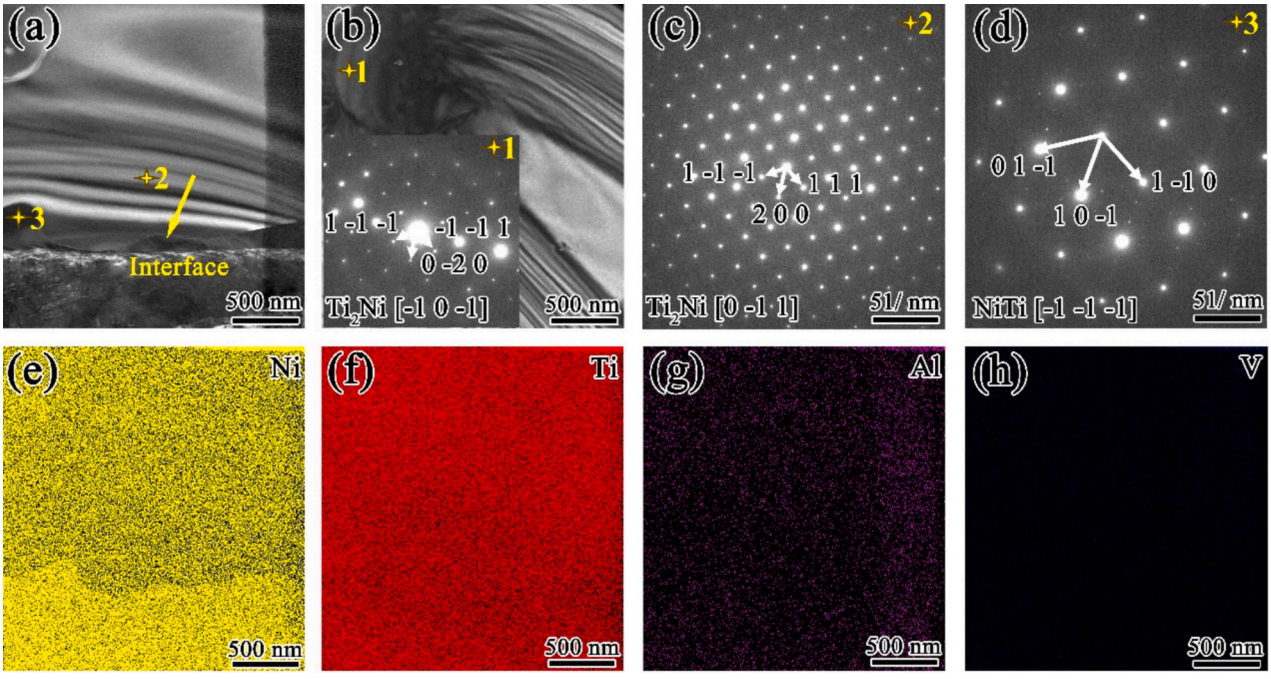

Fig. 9. TEM images and (SAED) images of NiTi FZ interfaces and transmittance maps of TEM-EDS results (a) HAADF image of NiTi FZ interfacial region; (b) Supplementary maps of (a); (b-d) SAD results of midpoints 1–3 in (a); and (e-h) EDS face scan results of (a).

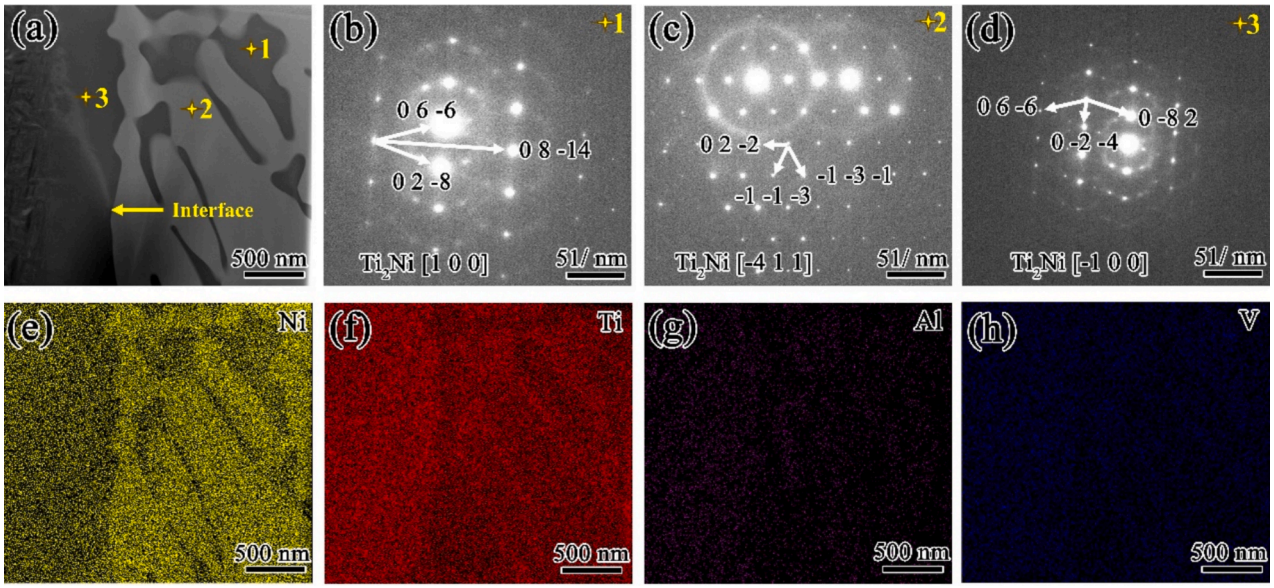

Fig. 10. TEM images and (SAED) images of the Ti6Al4V FZ interface and transmittance maps of TEM-EDS results (a) HAADF image of the Ti6Al4V FZ interfacial region; (b-d) SAD results of the mid-points 1–3 in (a); and (e-h) EDS face scan results of (a).

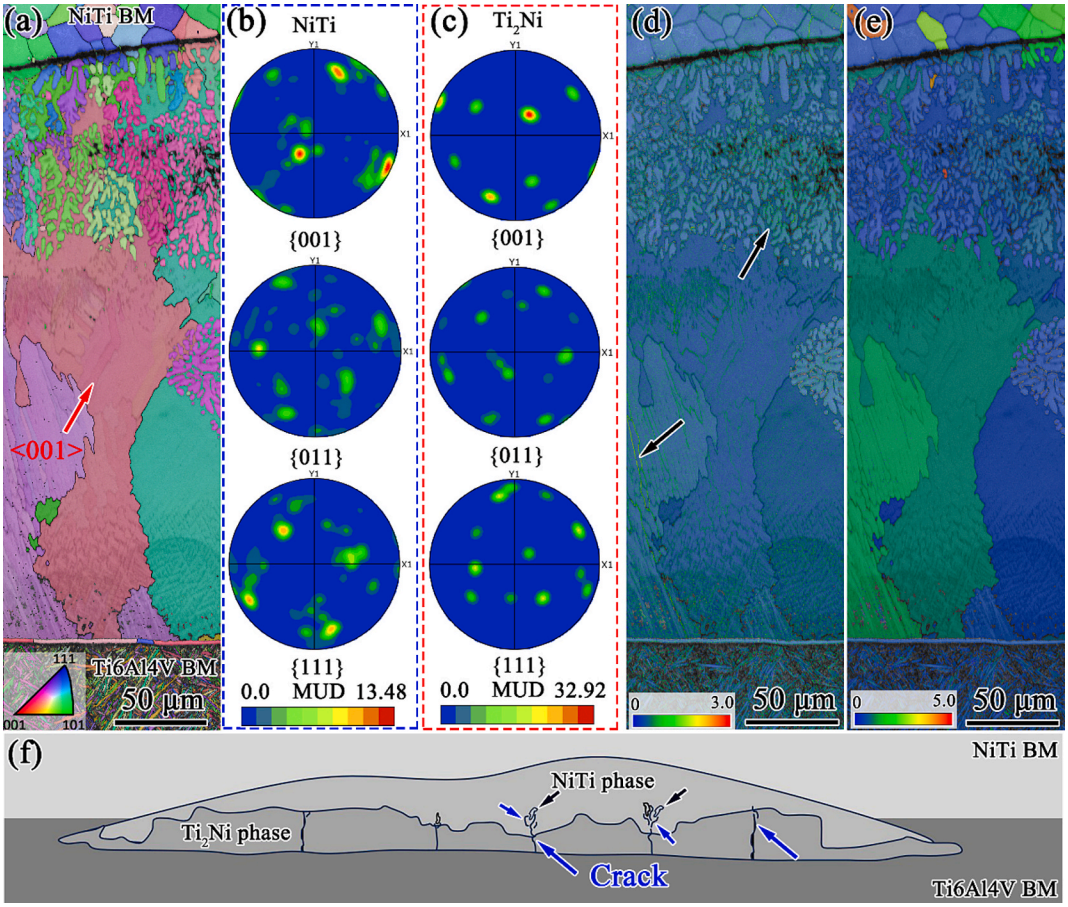

Fig. 11. EBSD results for the 7.5kA joint characterized by (a) IPF map, (b) PF map of the NiTi phase, (c) PF map of the Ti_2Ni phase, (d) KAM map, and (e) GOS map; (f) Schematic diagram of the formation of the NiTi/Ti6Al4V dissimilar joint during the RSW process.

growth orientation for FCC structures is typically along the < 001 > direction [45,46]. Moreover, since the maximum heat flow direction during the RSW process aligns with the preferred growth direction of the grains, these grains grow rapidly, resulting in a strong fiber texture of Ti_2Ni in the < 001 > direction.

The Kernel Average Misorientation (KAM) map, calculated by EBSD software, represents the average misorientation between each pixel and its nearest neighbor. Generally, regions with higher deformation exhibit

higher KAM values [47]. As indicated by the arrows in Fig. 11(d), the deformation is concentrated mainly in the interior of the large columnar grains on the Ti6Al4V side and at the grain boundaries of the smaller columnar grains on the NiTi side. These regions are more prone to strain localization and cracking, which aligns with the observed regions of transgranular and intergranular cracking, as discussed earlier. Grain Orientation Spread (GOS) reflects the plastic deformation capacity of grains, with lower GOS values indicating a more uniform strain distribution [48]. As shown in Fig. 11(e), regions with higher GOS values are predominantly located in the Ti_2Ni phase region, which is consistent with the KAM observations.

Fig. 11(f) illustrates a schematic of the microstructure formation during the RSW process of the NiTi/Ti6Al4V dissimilar joint. It can be seen that the bottom of the weld pool primarily consists of the Ti_2Ni phase, while the upper part of the weld pool is mainly composed of a mixed network of NiTi and Ti_2Ni intermetallic compounds (IMCs). Ti_2Ni is a brittle phase, and its extensive concentration leads to stress concentration, making it prone to cracking. Therefore, cracks typically initiate at the fusion line on the Ti6Al4V side and propagate toward the center of the weld, eventually terminating at the IMC network.

4.4. Relationship between Ti_2Ni phase and mechanical properties

As discussed in Sections 3.1 and 3.2, the lap-shear strength initially increases and then decreases with increasing welding current, while the number of cracks shows an opposite trend. This indicates that crack density is the primary factor influencing lap-shear strength. Additionally, the proportion of the Ti_2Ni phase also increases first and then decreases with increasing current, mirroring the trend of crack density. Cracks tend to initiate along the fusion line on the Ti6Al4V side and propagate towards the weld center, stopping near the bright white NiTi phase. Therefore, we conclude that the Ti_2Ni phase is the main factor responsible for crack formation, and its influence on crack density subsequently affects the lap-shear strength.

To further explore the impact of the RSW process on mechanical properties, we conducted nanoindentation tests on both the base metal and the welded joint, evaluating the superelastic response and microhardness of different regions (Fig. 12). As shown in Fig. 12(a), compared to the Ti6Al4V base metal (BM) with a recoverable depth of approximately 88.7 % after unloading, the NiTi BM, NiTi-side interface, NiTi fusion zone (FZ), Ti6Al4V FZ, and Ti6Al4V-side interface all exhibit typical superelastic curves. The superelastic response is attributed to the transformation of the B2 phase (austenite) to the B19′ phase (martensite) during loading and the reverse transformation during unloading. Although the NiTi/Ti6Al4V dissimilar joint shows superelastic behavior, the RSW process diminishes the superelastic performance of NiTi alloy, with recoverable depths of 70.9 %, 75.5 %, 81.3 %, 79.5 %, and 85.7 %, respectively. The gradual increase in recoverable depth percentage indicates a weakening of the superelastic response, consistent with the trend observed from the NiTi BM to the weld core. This is attributed to the increasing content of the Ti_2Ni phase from the NiTi interface to the Ti6Al4V interface, as well as grain coarsening and deviation in B2 orientation [23,49].

Fig. 12(b) presents the microhardness results for the BM and different regions within the joint. The average microhardness values increase from NiTi BM (5.9 GPa) to NiTi FZ (11.7 GPa) and then sharply rise to 16.2 GPa in the weld nugget due to the formation of the hard Ti_2Ni phase, before decreasing to 8.2 GPa in the Ti6Al4V FZ and 7.5 GPa in the Ti6Al4V BM. The sharp increase in microhardness in the weld nugget is attributed to the high volume fraction of the hard Ti_2Ni phase.

5. Conclusions

In this paper, the microstructure evolution and mechanical properties of resistance spot welding of NiTi shape memory alloy and Ti6Al4V dissimilar joints were investigated with the objective of weight reduction in aerospace manufacturing. Based on the above results and discussions, the following conclusions were obtained:

1. NiTi shape memory alloy and Ti6Al4V dissimilar joints were successfully jointed under the RSW process. With the continuous increase of welding current, the tensile shear load of dissimilar joints shows the trend of increasing first and then decreasing, when the welding current is 6.0 kA, the minimum value of tensile shear load is 2800 N; when the welding current is 7.5 kA, the tensile shear load reaches the maximum value of 4703 N. On the other hand, the cracks and Ti_2Ni phase showed a trend of decreasing and then increasing with the increase of current, and the number of cracks and Ti2Ni phase were the least in the case of a current of 7.5 kA, which was contrary to the trend of the change of the mechanical properties with the current, and proved that the cracks and the Ti_2Ni phase were the key factors affecting the present experiments.
2. The metallurgical reactions $L \rightarrow NiTi$ (congruent reaction), $L + NiTi \rightarrow Ti_2Ni$ (peritectic reaction), and $L \rightarrow \beta Ti + Ti_2Ni$ (eutectic reaction) existed in the NiTi/Ti6Al4V dissimilar joints on the basis of the results obtained by XRD aided with the analysis of the Ti-Ni binary phase diagram.
3. TEM microstructural characterization revealed that NiTi and Ti_2Ni phases were found at the NiTi side interface, while Ti_2Ni phase was found at the Ti6Al4V side interface. EBSD analysis indicates that the deformation of the dissimilar joint is mainly concentrated in the weld nugget, and is primarily distributed within the Ti_2Ni phase on the Ti6Al4V side and at the boundary between the NiTi phase and the Ti_2Ni phase. The areas with higher grain orientation spread values ($GOS > 1^{\circ}$) are also almost entirely within the Ti_2Ni phase, which is consistent with the crack initiation in the Ti_2Ni phase on the Ti6Al4V

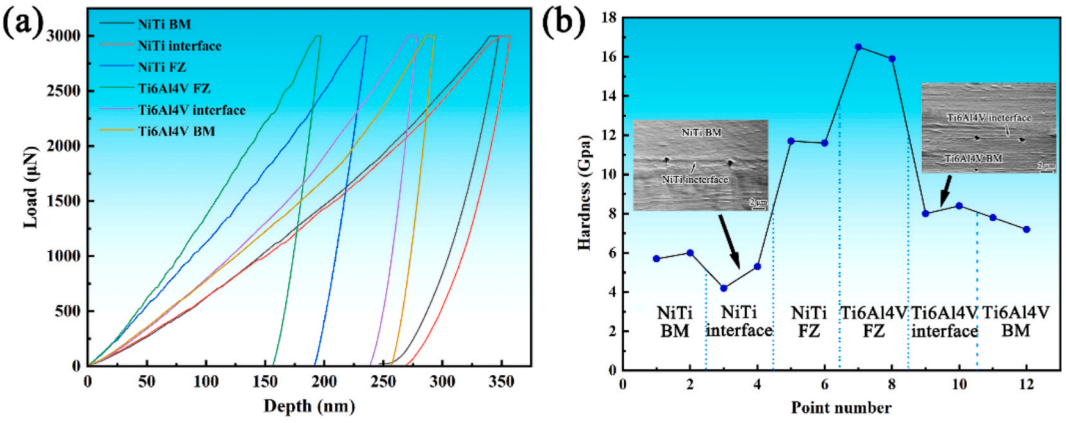

Fig. 12. (a) Nanoindentation data obtained from the BM and within the weld nugget; (b) microhardness results.

side of the joint and the slowing down or termination of the crack at the NiTi phase in the middle of the weld nugget.
4. Nanoindentation analysis showed that the welding process reduced the superelastic properties of NiTi due to grain coarsening and B2 orientation deviation, with an increase in the percentage of residual depth from 51.5 % to 69.1 %.

CRediT authorship contribution statement

Yihu Zang: Writing – review & editing, Writing – original draft, Visualization, Investigation, Data curation. **Jilin Xie:** Writing – review & editing, Supervision, Funding acquisition, Conceptualization. **Yuhua Chen:** Supervision, Resources, Funding acquisition, Conceptualization. **Min Zheng:** Supervision, Resources, Methodology, Conceptualization. **Xiaofang Liu:** Visualization, Supervision, Conceptualization. **Jiajia Shen:** Supervision, Resources, Conceptualization. **J.P. Oliveira:** Writing – review & editing, Methodology, Conceptualization.

Declaration of competing interest

The authors declare that they have no known competing financial interests or personal relationships that could have appeared to influence the work reported in this paper.

Acknowledgement

This work was supported by the National Natural Science Foundation of China (No. 52175326, No. U24A20117). Jiangxi Provincial Natural Science Foundation (No. 20242BAB23042, 20225BCJ23017)

Data availability

Data will be made available on request.

References

[1] E. Iaparova, L. Heller, O. Tyc, P. Sittner, Thermally induced reorientation and plastic deformation of B19' monoclinic martensite in nanocrystalline NiTi wires, Acta Mater. 242 (2023) 118477.
[2] K.F. Xu, J. Luo, C. Li, Y.L. Shen, C. Li, X. Ma, M.Q. Li, Mechanisms of stress-induced martensitic transformation and transformation-induced plasticity in NiTi shape memory alloy related to superelastic stability, Scr. Mater 217 (2022) 114775.
[3] Y.J. Ren, J.G. Du, B. Liu, Z.B. Jiao, Y.T. Tian, I. Baker, H. Wu, Microstructure, mechanical properties and biocompatibility of laser metal deposited Ti–23Nb coatings on a NiTi substrate, Mater. Sci. Eng. A 848 (2022) 143402.
[4] Z. Xiang, Q. Yang, T.H. Zhang, X.F. Shen, S.J. Hao, J. Chen, S.K. Huang, Tensile mechanical behavior of functionally graded NiTi alloy manufactured via laser powder bed fusion, Mater. Sci. Eng. A 914 (2024) 147119.
[5] S. Parvizi, S.M. Hashemi, S. Moein, 19 - NiTi shape memory alloys: properties, Nickel-Titanium Smart Hybrid Mater. (2022) 399–426.
[6] S.L. Lu, Z.J. Zhang, R. Liu, X.H. Zhou, X.G. Wang, B.N. Zhang, X.M. Zhao, J. Eckert, Z.F. Zhang, Optimal tensile properties of laser powder bed fusion hereditary basket-weave microstructure in additive manufactured Ti6Al4V, Addit. Manuf. 59 (2022) 103092.
[7] L. Bhandari, V. Gaur, On study of process induced defects-based fatigue performance of additively manufactured Ti6Al4V alloy, Addit. Manuf. 60 (2022) 103227.
[8] P.F. Jiang, M.H. Nie, X.M. Zong, X.B. Wang, Z.K. Chen, C.Z. Liu, J.Z. Teng, Z. H. Zhang, Microstructure and mechanical properties of TC4/NiTi bionic gradient heterogeneous alloy prepared by multi-wire arc additive manufacturing, Mater. Sci. Eng. A 866 (2023) 144678.
[9] J.P. Oliveira, B. Panton, Z. Zeng, C.M. Andrei, Y. Zhou, R.M. Miranda, F.M. B. Fernandes, Laser joining of NiTi to Ti6Al4V using a Niobium interlayer, Acta Mater. 105 (2016) 9–15.
[10] J.L. Xie, Y.H. Zhou, C.P. Zhou, X.P. Li, Y.H. Chen, Microstructure and mechanical properties of Mg–Li alloys fabricated by wire arc additive manufacturing, J. Mater. Res. Technol. 29 (2024) 3487–3493.
[11] L. Quintino, L. Liu, A. Hu, R.M. Miranda, Y. Zhou, Fracture analysis of Ag nanobrazing of NiTi to Ti alloy, Solda. Insp. 18 (2013) 281–286.
[12] R.M. Miranda, E. Assunção, R.J.C. Silva, J.P. Oliveira, L. Quintino, Fiber laser welding of NiTi to Ti-6Al-4V, Inter J. Adva Manuf. Technol. 81 (2015) 1533–1538.
[13] P. Song, Y. Zhu, W. Guo, P. Qu, H. Kang, K. Wen, Mechanism of crack formation in the laser welded joint between NiTi Shape memory alloy and TC4, Rare Met. Mater. Eng. 42 (2013) 6–9.
[14] X.W. Zhou, Y.H. Chen, Y.D. Huang, Y.Q. Mao, Y.Y. Yu, Effects of niobium addition on the microstructure and mechanical properties of laser-welded joints of NiTiNb and Ti6Al4V alloys, J. Alloys Compd. 735 (2018) 2616–2624.
[15] S. Simões, F. Viana, A.S. Ramos, M.T. Vieira, M.F. Vieira, Reaction zone formed during diffusion bonding of TiNi to Ti6Al4V using Ni/Ti nanolayers, J. Mater. Sci. 48 (2013) 7718–7727.
[16] J.L. Xie, Y.H. Chen, L.M. Yin, T.M. Zhang, S.L. Wang, L.T. Wang, Microstructure and mechanical properties of ultrasonic spot welding TiNi/Ti6Al4V dissimilar materials using pure Al coating, J. Manuf. Process 64 (2021) 473–480.
[17] K.P. Zhang, L.J. Wu, C.W. Tan, Y.M. Sun, B. Chen, X.G. Song, Influence of Al-Si coating on resistance spot welding of Mg to 22MnB5 boron steel, J. Mater. Process. Technol. 271 (2019) 23–35.
[18] L. Liu, L. Xiao, J.C. Feng, Y.H. Tian, S.Q. Zhou, Y. Zhou, The mechanisms of resistance spot welding of magnesium to steel, Metall. Mater. Trans. A 41 (2010) 2651–2661.
[19] C. Schmal, G. Meschut, Refill friction stir spot and resistance spot welding of aluminium joints with large total sheet thicknesses (III-1965-19), Weld. World 64 (9) (2020) 1471–1480.
[20] A. Chabok, H.T. Cao, E.V.D. Aa, Y.T. Pei, New insights into the fracture behavior of advanced high strength steel resistance spot welds, J. Mater. Process. Technol. 301 (2022) 117433.
[21] C.Q. Zhang, J.D. Robson, O. Ciuca, P.B. Prangnell, Microstructural characterization and mechanical properties of high power ultrasonic spot welded aluminum alloy AA6111–TiAl6V4 dissimilar joints, Mater. Charact. 97 (2014) 83–91.
[22] H. Fujii, Y. Sun, H. Kato, K. Nakata, Investigation of welding parameter dependent microstructure and mechanical properties in friction stir welded pure Ti joints, Mater. Sci. Eng. A 527 (15) (2010) 3386–3391.
[23] K. Zhang, A. Shamsolhodaei, A. Ghatei-Kalashami, J.P. Oliveira, C. Zang, N. Schell, J. Li, A.R.H. Midawi, J.G. Lopes, J. Yan, P.E.J. Rivera-Dıaz-del-Castillo, P. Peng, Y. N. Zhou, Revealing microstructural evolution and mechanical properties of resistance spot welded NiTi-stainless steel with Ni or Nb interlayer, J. Mater. Sci. Technol. 180 (2024) 160–173.
[24] Y.Q. Zhang, S.Y. Jiang, Y.N. Zhao, M. Tang, Influence of cooling rate on phase transformation and microstructure of Ti-50.9% Ni shape memory alloy, T. Nonferr. Metal. Soc China 22 (11) (2012) 2685–2690.
[25] H. Niu, H.C. Jiang, M.J. Zhao, L.J. Rong, Effect of interlayer addition on microstructure and mechanical properties of NiTi/stainless steel joint by electron beam welding, J. Mater. Sci. Technol. 61 (2021) 16–24.
[26] J. Vannod, M. Bornert, J.E. Bidaux, L. Bataillard, A. Karimi, J.M. Drezet, M. Rappaz, A. Hessler-Wyser, Mechanical and microstructural integrity of nickel–titanium and stainless steel laser joined wires, Acta Mater 59 (17) (2011) 6538–6546.
[27] H.M. Li, D.Q. Sun, X.L. Cai, P. Dong, X.Y. Gu, Laser welding of TiNi shape memory alloy and stainless steel using Co filler metal, Opt Laser Technol 45 (2013) 453–460.
[28] Y.H. Chen, Y.Q. Mao, W.W. Lu, P. He, Investigation of welding crack in micro laser welded NiTiNb shape memory alloy and Ti6Al4V alloy dissimilar metals joints, Opt Laser Technol 91 (2017) 197–202.
[29] X. Cui, S. Zhang, Z.Y. Wang, C.H. Zhang, C.L. Ni, C.L. Wu, Microstructure and fatigue behavior of 24CrNiMo low alloy steel prepared by selective laser melting, Mater. Sci. Eng. A 845 (2022) 143215.
[30] A. Dębski, W. Gąsior, A. Sypień, A. Góral, Enthalpy of formation of intermetallic phases from Al–Ni and Al–Ni–Ti systems, Intermetallics 42 (2013) 92–98.
[31] F.C. Liu, X. Lin, H. Leng, J. Cao, Q. Liu, C.P. Huang, W.D. Huang, Microstructural changes in a laser solid forming Inconel 718 superalloy thin wall in the deposition direction, Opt Laser Technol 45 (2013) 330–335.
[32] W.M. Steen, J. Mazumder, Laser material processing, Springer S BM (2010).
[33] X. Tang, S. Zhang, X. Cui, C.H. Zhang, Y. Liu, J.B. Zhang, Tribological and cavitation erosion behaviors of nickel-based and iron-based coatings deposited on AISI 304 stainless steel by cold metal transfer, J. Mater. Res. Technol. 9 (3) (2020) 6665–6681.
[34] A. Rahman, M. Cavalli, Diffusion bonding of commercially pure Ni using Cu interlayer, Mater Charact 69 (2012) 90–96.
[35] S. Li, H. Hassanin, M.M. Attallah, N.J. Adkins, K. Essa, The development of TiNi-based negative Poisson's ratio structure using selective laser melting, Acta Mater. 105 (2016) 75–83.
[36] D.J. Wu, C.C. Song, T.D. Di, F.Y. Niu, G.Y. Ma, Intermetallic regulation mechanism of inconel 718/Ti6Al4V composite by novel follow-up ultrasonic assisted laser additive manufacturing, Compos . B: Eng. 235 (2022) 109736.
[37] A.R. Pelton, J. Dicello, S. Miyazaki, Optimisation of processing and properties of medical grade Nitinol wire, Minim Invasiv Ther 9 (2) (2000) 107–118.
[38] D.A. Porter, K.E. Easterling, Phase transformations in metals and alloys, 2009.
[39] J.H. Lee, J.H. wang, D.J. Lee, H.J. Ryu, S.H. Hong, Enhanced mechanical properties of spark plasma sintered NiTi composites reinforced with carbon nanotubes, J. Alloys Compd. 617 (2014) 505–510.
[40] R. Mackay, G.J. Miller, H.F. Franzen, New oxides of the filled-Ti2Ni type structure, J. Alloys Compd. 204 (1–2) (1994) 109–118.
[41] S. Chatterjee, T.A. Abinandanan, K. Chattopadhyay, Microstructure development during dissimilar welding: Case of laser welding of Ti with Ni involving intermetallic phase formation, J. Mater. Sci. 41 (2006) 643–652.
[42] A. Shamsolhodaei, J.P. Oliveira, N. Schell, E. Maawad, B. Panton, Y.N. Zhou, Controlling intermetallic compounds formation during laser welding of NiTi to 316L stainless steel, Intermetallics 116 (2020) 106656.
[43] C. Wei, L.C. Liu, H.T. Cao, X.L. Zhong, X. Xu, Y.C. Gu, D.X. Cheng, Y.H. Huang, Z. Q. Li, W. Guo, Z. Liu, L. Li, Cu10Sn to Ti6Al4V bonding mechanisms in laser-based

powder bed fusion multiple material additive manufacturing with different build strategies, Addit. Manuf. 51 (2022) 102588.
[44] Y. Lee, M. Nordin, S.S. Babu, D.F. Farson, Effect of fluid convection on dendrite arm spacing in laser deposition, Metall. Mater. Trans. B 45 (4) (2014) 1520–1529.
[45] H.L. Wei, J. Mazumder, T. DebRoy, Evolution of solidification texture during additive manufacturing, Sci. Rep. 5 (1) (2015) 16446.
[46] Y.Z. Zhou, A. Volek, N.R. Green, Mechanism of competitive grain growth in directional solidification of a nickel-base superalloy, Acta Mater. 56 (11) (2008) 2631–2637.
[47] J. Konrad, S. Zaefferer, D. Raabe, Investigation of orientation gradients around a hard Laves particle in a warm-rolled Fe3Al-based alloy using a 3D EBSD-FIB technique, Acta Mater. 54 (5) (2006) 1369–1380.
[48] S.R. Liu, Y.K. Xiong, J.F. Zhao, B.X. Liu, W.W. Wu, X. Zhang, Nonlocal crystal plasticity and damage modeling of dual-heterostructured steel for strengthening and failure analysis, Int. J. Plast. 187 (2025) 104270.
[49] A. Shamsolhodaei, A. GhateiKalashami, A. Safdel, A.R.H. Midawi, M.A. Elbestawi, P. Peng, Y.N. Zhou, Resistance spot welding of NiTi shape memory alloy sheets: Microstructural evolution and mechanical properties, J. Manuf. Process 81 (2022) 467–475.